First–Principles Parameter–Free Modeling of n– and p–FET Hot–Carrier Degradation

M. Jech*, S. Tyaginov°, B. Kaczer°, J. Franco°, D. Jabs†, C. Jungemann†, M. Waltl*,•,T. Grasser*

*Institute for Microelectronics (•CDL for Single–Defect Spectroscopy), TU Wien, Austria °*imec*, Leuven, Belgium †RWTH, Aachen, Germany

***Abstract*— We use an ab initio quantum chemistry approach to reveal and describe the intricate physics underlying hot–carrier degradation (HCD). We identify a resonance scattering mechanism to be responsible for the interaction of energetic carriers with the Si–H bond at the Si/SiO_2 interface. Within this formulation carriers tunnel into an available resonance state and produce multiple vibrational excitations of the bond upon inelastic relaxation. Since in our approach all model parameters are rigorously obtained from ab initio calculations, it is essentially free of fitting parameters or assumptions. Our ab initio based framework describes HCD in *both n– and p–FETs* and also clearly reveals the differences in the HCD mechanisms between them. We finally validate the model against measurement data for n– and p–channel transistors.**

I. Introduction

Hot–carrier degradation (HCD) has been continuously reported over the past decade to be among the most troublesome reliability issues [1, 2]. Despite its significance in modern technology nodes, the physics behind this detrimental phenomenon are not yet fully understood. While it is widely accepted that HCD is due to broken Si–H bonds at the Si/SiO_2 interface, the actual details of the defect creation mechanisms have remained speculative.

A major step towards understanding and modeling HCD was achieved in a series of papers by the group of Hess almost 20 years ago [3–6]. The key idea of their proposed model is to link the information on how carriers are distributed over energy, provided by the carrier **energy distribution function** (**EDF**), with two different but interacting regimes for defect creation. According to Hess, electron induced excitation and eventually breakage of Si–H can be due to either a **single particle** (**SP**) or a **multiple particle** (**MP**) mechanism. The SP process accounts for the high energy fraction of the carrier ensemble where a single carrier triggers the dissociation of hydrogen. This regime is based on the physical context of an electronic excitation of one of the valence electrons of the Si–H bond. On the other hand, the MP mechanism describes a subsequent vibrational excitation of the Si–H eigenstates. These concepts have served as a basis for further developments and are still the essence of state–of–the–art modeling approaches [7–9]. However, no details on the physical principles behind the electron/Si–H bond interaction have been given so far, despite its importance in recent modeling results.

Developing a physically consistent model to describe the interaction of energetic carriers with bonds at the semiconductor–insulator interface is, therefore, of special relevance, particularly with regards to future technologies [10]. We have developed a generally valid formulation describing bond excitation and breaking mechanisms using state–of–the–art *ab initio* based quantum chemistry calculations which provides a fundamental understanding of the degradation dynamics at a device level.

II. Modeling Approach

The **dissociation dynamics** of the Si–H bond at the Si/SiO_2 interface are still largely unknown due to the complex interface between the crystalline silicon substrate and the amorphous SiO_2 oxide. Extensive theoretical work by Tuttle *et al.* [11, 12] and Van de Walle *et al.* [13, 14], who investigated hydrogen related configurations in various silicon models, suggests two H configurations for creating an interfacial Si dangling bond: the antibonding site (AB–site), which is a $180°$ flipped position of the H, and a bond–center site (BC–site), where the hydrogen is between the next Si–Si bond. However, there is still no clear picture regarding the dissociation kinetics which explains the experimental data by Brower [15] and Stesmans [16] showing an activation barrier between $2.56\,\mathrm{eV}$ and $2.83\,\mathrm{eV}$. In order to take a fresh look we employed *ab initio* density functional theory (DFT) calculations on a Si/SiO_2 model which contains one Si–H bond at the interface, see Fig. 1. The DFT package CP2k together with the PBE0 hybrid functional and a mixed Gaussian basis set provides an accurate description of the system. Nudged elastic band calculations, connecting the Si–H equilibrium configuration with the AB–site and the next but one BC-site respectively, were used to optimize the reaction path and determine the minimum energy path. Fig. 2 shows the resulting transition barriers along the reaction path together with the respective atomistic structure and the change of the projected density of electronic states. One can clearly see that this AB–site (Path I) is a dead–end in the reaction dynamics with no active defect levels and would not facilitate Si–H dissociation. However, Path II, where the H moves towards an adjacent Si and eventually between the next but one Si-Si bond, forming a BC–site, shows the desired characteristics. With a forward barrier of $2.77\,\mathrm{eV}$ and Si dangling bond trap levels within the Si band gap, the dissociation trajectory properly reflects experimental data.

In order to supply the required energy for bond breaking, carriers can trigger various **excitation mechanisms**, depending on their energy. As was investigated by the group of Avouris [17, 18], highly energetic electrons can indeed result in an **electronic excitation** of one of the bonding electrons, similar to the previously mentioned SP mechanism. However, in the case of Si–H bonds, such a transitions requires at least a carrier energy of $6.5\,\mathrm{eV}$, which is therefore not applicable to HCD in scaled devices. On the other hand, experimentally it was found that carriers with energies between $2\,\mathrm{eV}$ and $5\,\mathrm{eV}$ can still excite the vibrational states of the Si–H bond [19]. Together with the strong current dependence observed, such a mechanism agrees well with the characteristic features of HCD in MOSFETs. Theoretically, this can be described within a **resonant scattering** model, where carriers tunnel into an adsorbate resonance and upon inelastic relaxation produce multiple vibrational excitations. The resonances responsible for such a mechanism have been calculated by Stokbro *et al.* [20, 21] and are in good agreement with our own values reported in Fig. 3. The electronic resonance is centered around $E_{\mathrm{res}} = 3.67\,\mathrm{eV}$ above E_{C} with an average width of $\Delta = 1.1\,\mathrm{eV}$, whereas the accessible state for holes is $E_{\mathrm{res}} = -4.54\,\mathrm{eV} \pm 0.56\,\mathrm{eV}$ below E_{V}. Transition rates between the eigenstates can be calculated by utilizing the coherent vibrational excitation model proposed by Persson *et al.* [22], which includes not only neighbouring transitions ($\Delta i = \pm 1$) but also overtone transitions to higher eigenstates ($\Delta i = \pm 2, \pm 3, \pm 4, \cdots$). Approximating the DFT bonding and resonance potential by a harmonic oscillator, see Fig. 4, it can be assumed that an electron with incident energy ϵ can induce an excitation from state $|\phi_i\rangle$ to $|\phi_f\rangle$ via the vibrational eigenstate $|\psi_j\rangle$ of the resonance, see (1). The formula takes into account the EDF $f(\epsilon)$, the density of states $g(\epsilon)$, the carrier velocity $v(\epsilon)$ as well as an energy dependent cross section $\sigma(\epsilon)$. Contrary to previous model formulations, where the cross section is an empirical Keldysh–like expression $\sigma(\epsilon) = \sigma_0(\epsilon - \epsilon_{\mathrm{th}})^p$ with $p_{\mathrm{MP}} = 1$ and $p_{\mathrm{SP}} = 11$ [6, 7, 27], the quantum–chemistry formulation utilized in this work allows for a physically meaningful interpretation: It is the probability of the transition from $|\phi_i\rangle$ to $|\phi_f\rangle$ via the resonance state $|\psi_j\rangle$, given by the overlap of the wavefunctions, weighted by the resonance position represented by a Lorentzian, see Fig. 4 and Fig. 5. A detailed comparison is given in Fig. 5. While the empirical Keldysh–like expression does not depend on the current eigenstate and only considers direct neighbouring transitions, our formulation includes the current excitation state (via $E_{\mathrm{res}} + \epsilon_i - \epsilon_j$) and also considers transitions to higher excited states. Note that within this model overtone transitions can potentially have a higher excitation probability, see the upper left panel of Fig. 5. Interestingly, the presented resonant scattering model maps the previously discussed SP and MP processes onto a single physical

mechanism, since it accounts for neighbouring transitions (ladder climbing, MP) as well as transitions to higher excited states which potentially cause direct dissociation (overtone transitions, SP). Besides its physical interpretation it further allows for an intuitive understanding of another peculiarity of HCD. Reports show that HCD in nMOS devices is more pronounced than in pMOSFETs [23–25]: As shown in Fig. 3, the accessible resonance state for holes is higher in energy than for electrons, thus it is less likely for holes to trigger bond excitation and dissociation.

Another important parameter which strongly determines the dissociation dynamics is the vibrational relaxation time $\tau_{1,0}$. Previous studies report values of $\tau_{1,0} = 1.5\,\text{ns}$ for the Si–H stretching mode on a *silicon surface* and attribute the long lifetime to the discrepancy between the Si–H stretching frequency ($\sim 250\,\text{meV}$) and the largest Si bulk phonon mode ($\sim 60\,\text{meV}$) [26]. Thus, the energy relaxation is dominated by a multiphonon path which effectively increases the lifetime. The different atomistic structure at the Si/SiO_2 interface as well as the dissociation trajectory proposed in Fig. 2 potentially influence the lifetime. Our calculated phonon mode spectrum of the Si/SiO_2 interface system shows a broader normal–mode spectrum together with a reduced mismatch to the fundamental frequency of the bonding potential ($\Delta_{1,0} = 190\,\text{meV}$). However, the eigenfrequency is still outside of the phonon bath, rendering it compatible to higher vibrational lifetimes of the Si–H stretching mode, which have a lifetime of $\tau \sim 1\,\text{ns}$ [26]. We therefore used $\tau_{1,0} = 1.0\,\text{ns}$ and allowed a physically reasonable variation of $\pm 0.5\,\text{ns}$ within our framework. Finally, $\tau_{1,0} = \gamma^{-1}$ together with (3) was used to calculate lifetimes for higher excited states as well as different temperatures, see Fig 6.

Previous HCD model approaches considered the interaction of the Si–H bond with an electric field as an important component which significantly reduces the dissociation barrier. However, this assumption has not been rigorously justified yet. Effective dipole moments between $0.8\,\text{eÅ}$ and $5.5\,\text{eÅ}$ can be found in the literature [27, 28], which would result in an effective barrier lowering between $0.1\,\text{eV}$ and $0.5\,\text{eV}$ at $10\,\text{MV/cm}$. Following the approach in [29], one can extract the change of the dipole moment vector along the reaction coordinate at zero field using DFT calculations. Defining an effective dipole moment $\boldsymbol{\mu}_{\text{eff}}$, the change of potential due to an applied field is given by $\Delta E = -\boldsymbol{\mu}_{\text{eff}} \cdot F$, see Fig. 7. Accounting for a field across the interface (the z–component) yields $\mu_{\text{eff}} = 0.24\,\text{eÅ}$, which leaves the transition state *virtually unaffected* and its change can be neglected, see Fig. 7, contrary to conventional assumption.

Finally, for all aforementioned processes, namely resonance scattering mechanism and vibrational relaxation, transition rates $\Gamma_{i,f}$ can be calculated and a total (de-) excitation rate $\Gamma_{i,f}^{\text{tot}}$ can be defined, see (4). Subsequently, the new quasi–equilibium solution of the Pauli Master equation, see (5), can be calculated which yields the individual state population P_i of the Si–H potential. Including the first continuum state (the first state above the barrier), the final dissociation rate Γ_{D} can be written as the state population P_i times the rate from i to the continuum state $f+1$, see (6). Knowing the dissociation rate Γ_{D}, the evolution of broken and intact Si–H bonds with stress time is given by reaction (7).

III. Results & Discussions

Measurements in this work were performed on two different devices, a pMOSFET technology employing a $2.2\,\text{nm}$ SiON thick insulator with a gate length of $100\,\text{nm}$ and an SiON nMOSFET with a gate length of $65\,\text{nm}$. Both devices have an operating voltage of $|V_{\text{DD}}| = 1.5\,\text{V}$ and have been subjected to the respective worst case stress conditions, namely $\text{V}_\text{G} = -1.5\,\text{V}$ and $\text{V}_\text{D} = -1.8\,\text{V}, -2.3\,\text{V}, -2.8\,\text{V}$ for the pMOS and $\text{V}_\text{G} = \text{V}_\text{D} = 1.8\,\text{V}, 2.0\,\text{V}, 2.2\,\text{V}$ for the nMOS device. To monitor the degradation trend we recorded $\Delta I_{\text{D,lin}}(t)$ traces up to $10\,\text{ks}$ of stress.

In a first step we self–consistently solved the bipolar Boltzmann transport equation (BTE) [30, 31] on the calibrated 2D structures obtained from process simulation. The considered scattering mechanisms are acoustical and optical phonon scattering, impurity scattering as well as impact ionization with secondary carrier generation. The results for both devices and all stress conditions are shown in Fig. 9. Clearly visible is the characteristic accumulation of highly energetic majority carriers at the drain end of the channel for both devices. As expected, increasing the stress conditions results in a more pronounced high energy fraction of the EDF for holes (pMOS) and electrons (nMOS). However, while the EDFs of the secondary generated holes in the nMOS remain almost unchanged for the given stress conditions, the electron EDFs in the pMOS significantly change for higher stress bias. Thus, particularly for the highest drain bias condition, $\text{V}_\text{D} = -2.8\,\text{V}$, electrons can be expected to contribute to the total device degradation in pFETs, since their EDFs are populated for energies up to $4\,\text{eV}$ along the channel region. The EDFs have been used within our modeling framework described above to calculate interface state profiles $N_{\text{it}}(x)$ which were subsequently used to simulate $\Delta I_{\text{D,lin}}(t)$ traces. To give detailed insights, Fig. 10. shows the spatial distribution of the calculated $N_{\text{it}}(x)$ profile along the Si/SiON interface. Clearly visible are the characteristic peaks at the drain end of the channel for both devices, nMOS and pMOS, for all three stress conditions. This particular feature of HCD can evidently be explained by the hot carrier ensemble at the drain end, see Fig. 9 and Fig. 10. However, while for nMOSFETs the damaged region continuously extends from the drain end towards the channel region, the buildup of a second peak in the channel region is visible for increasing bias in the pMOS device [32, 33]. To understand this behaviour in more detail, the individual bond breaking rates Γ_{break} for the corresponding carriers are shown in the lower panel of Fig. 10. Apparently, in the nMOS degradation is exclusively determined by electrons, whereas in the pMOS a significant contribution is due to the secondary generated electrons. Furthermore, by comparing the individual rates, Fig. 10, to the EDFs shown in Fig. 11, one can see the impact of the different resonance states for electrons and holes discussed in Sec. II. Although the EDF_e (nMOS) and EDF_h (pMOS) at the drain end are comparable, the electron rates are almost two orders of magnitude larger, see Fig. 10. On the other hand, in the channel region secondary generated holes (nMOS) do not contribute to the degradation at all, while electrons created by impact ionization (pMOS) dominate the damage, see Fig. 10 and Fig. 11. Resonance based excitations are the key ingredient in our modeling framework which allow us to understand the different degradation characteristics induced by electrons and holes and also properly capture the degradation trends, see Fig. 12. We want to emphasize that throughout the simulations a unique, albeit slightly optimized, parameter set was used, see Fig. 13. However, even the *ab inito* based values summarized in Fig. 13 result only in small deviations from the optimized parameters, see Fig. 12, given our approach predictive qualities.

IV. Conclusion

We have presented a modeling framework to capture the nature of hot–carrier degradation which reveals new and interesting physics. We have shown that the previously used MP and SP mechanisms are actually a manifestation of the same physical interaction, a resonance scattering excitation. Interestingly, this idea was already proposed in one of the pioneering papers by the group of Hess, however not further pursued by recent developments. Besides its physically meaningful concept, the model is virtually free of fitting parameters as shown by our analysis. Furthemore, it naturally provides an explanation for why the created *damage for nMOS is larger than for pMOS*: The accessible *resonance state for holes is higher in energy* and therefore it is less likely for holes to induce excitations of the Si–H bond.

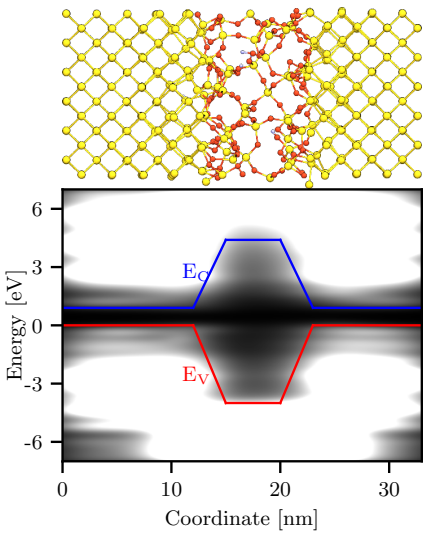

Fig. 1: A DFT simulation of an interface model between Si and amorphous SiO_2 which contains ~ 500 atoms. The band gaps of Si as well as of a–SiO_2 are well represented by our calculations ($E_{g,Si} = 0.9\,eV$ and $E_{g,SiO_2} = 8.7\,eV$).

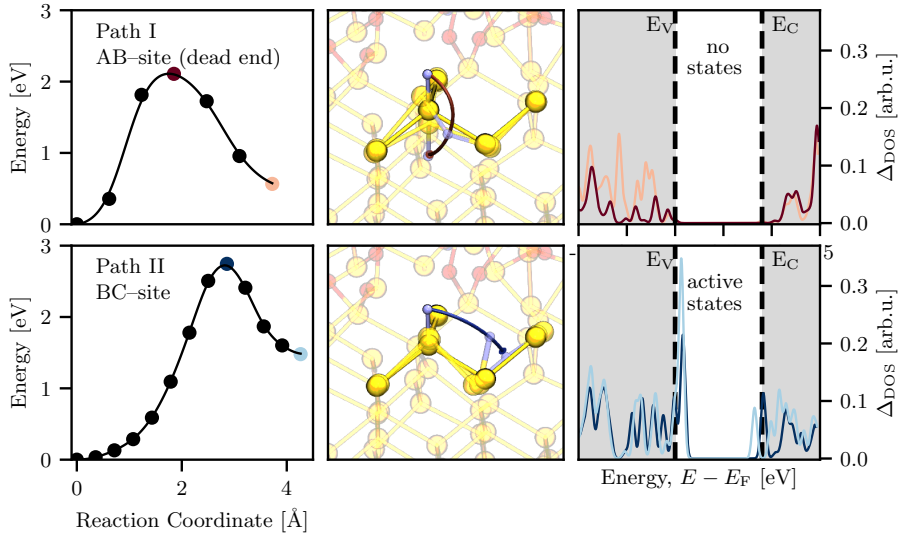

Fig. 2: Climbing image nudged elastic band simulations investigating the minimum energy path between the intact Si–H configuration and the flipped AB–site (upper panel, Path I) and the BC–site (lower panel, Path II). Path I exhibits an energy barrier of 2.2 eV, however, no electronic states appear in the band gap indicating that the Si–H bond will remain intact. In contrast, Path II requires 2.77 eV for the forward reaction and introduces localized states in the Si band gap and therefore facilitates bond dissociation.

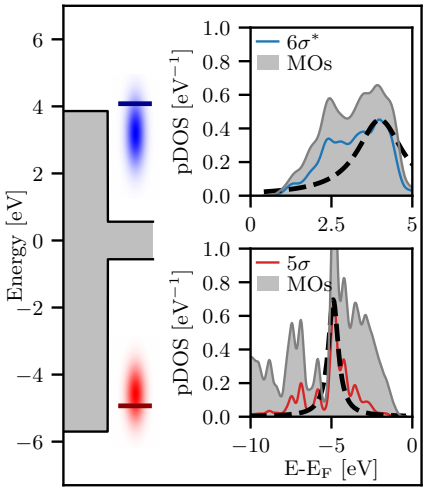

Fig. 3: The electron and hole resonance level in the context of a Si/SiO_2 interface. The coloured lines in the insets show the projections of the resonance states onto the Si conduction and valence band (grey areas). The dashed lines are Lorentzian fits to extract the peak positions as well as their broadening. Additionally the results of Stokbro *et al.* are shown as the coloured bars.

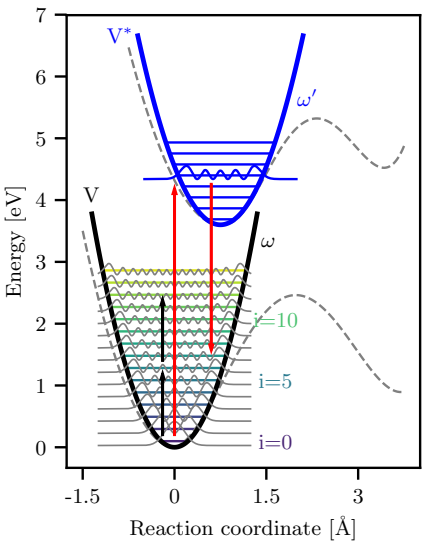

Fig. 4: Schematics showing the resonant scattering interaction. In a first step the carrier creates an excited charged complex by temporarily localizing into a resonance state (upwards red arrow), denoted by V*. Inelastic relaxation (downwards red arrow) allows for overtone transitions and the potential is left in a vibrationally excited state.

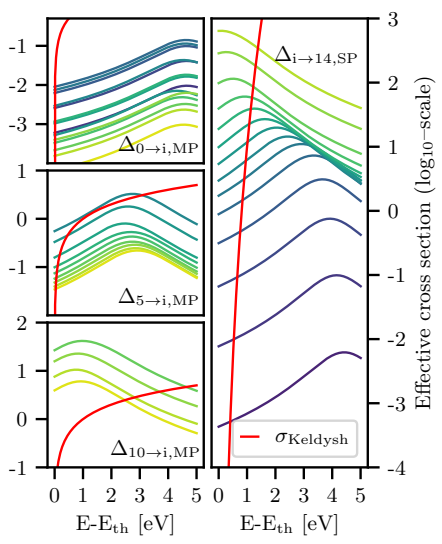

Fig. 5: Regardless of the excitation state of the bond, the previously used Keldysh cross section is a function of the incident carrier energy. In contrast, our quantum–dynamical formulation takes the current vibrational state into account and allows for overtone transitions weighted by the wavefunction overlap and the resonance position represented by a Lorentzian.

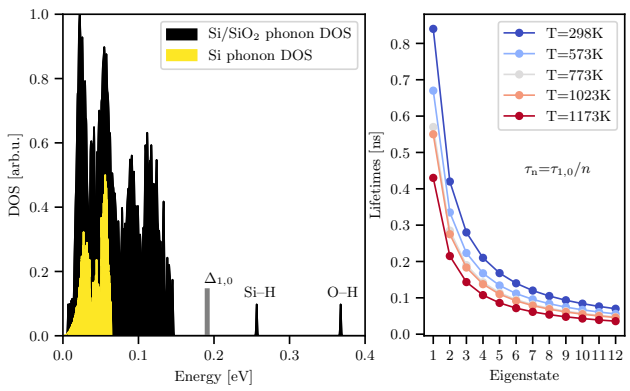

Fig. 6: Phonon density of states for Si bulk and an Si/SiO_2 interface obtained from DFT. The main part of the interface DOS, related to collective vibrations, is much broader compared to c–Si. This potentially allows for a more efficient coupling of $\Delta_{1,0}$ to the phonon bath. The right panel shows the lifetimes calculated from (3) for different temperatures.

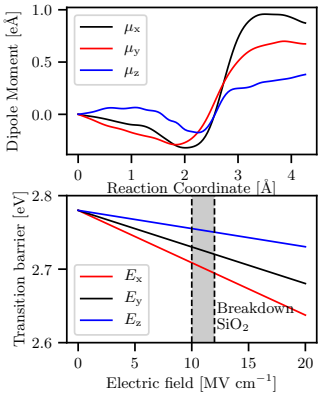

Fig. 7: The components of the dipole moment vector $\boldsymbol{\mu}$ along the reaction coordinate for Path II and the calculated reduction of the transition barrier.

$$(1)\ \Gamma^{res}_{i,f} = \frac{4\Delta_r^2}{\pi}\int_\epsilon \mathrm{d}\epsilon f(\epsilon)g(\epsilon)v(\epsilon)\sigma(\epsilon)$$

$$(2)\ \sigma(\epsilon) = \sigma_0\left|\sum_j \frac{\langle\phi_f|\psi_j\rangle\langle\psi_j|\phi_i\rangle}{E_r - \epsilon + \epsilon_i - \epsilon_j + i\Delta_r}\right|^2$$

$$(3)\ \Gamma^{vib}_{i,f} = \frac{2}{\hbar}|\langle\phi_f|f(q)|\phi_i\rangle|^2 m\gamma\omega_{i,f}$$

$$(4)\ \Gamma^{tot}_{i,f} = \Gamma^{res}_{i,f} + \Gamma^{vib}_{i,f}$$

$$(5)\ \frac{\mathrm{d}P_i}{\mathrm{d}t} = \sum_i P_i\Gamma^{tot}_{i,j} = 0$$

$$(6)\ \Gamma_D = \sum_i P_i\Gamma^{tot}_{i,f+1}$$

$$(7)\ \frac{\mathrm{d}N_{it}}{\mathrm{d}t} = (N_0 - N_{it})\Gamma_D - N_{it}^2\Gamma_P$$

Fig. 8: Equations describing our new quantum-dynamic model. While in previous models an empirical Keldysh–like fitting model for σ was used, our approach results in an accurate and physical description of the desorption process via (2)-(6).

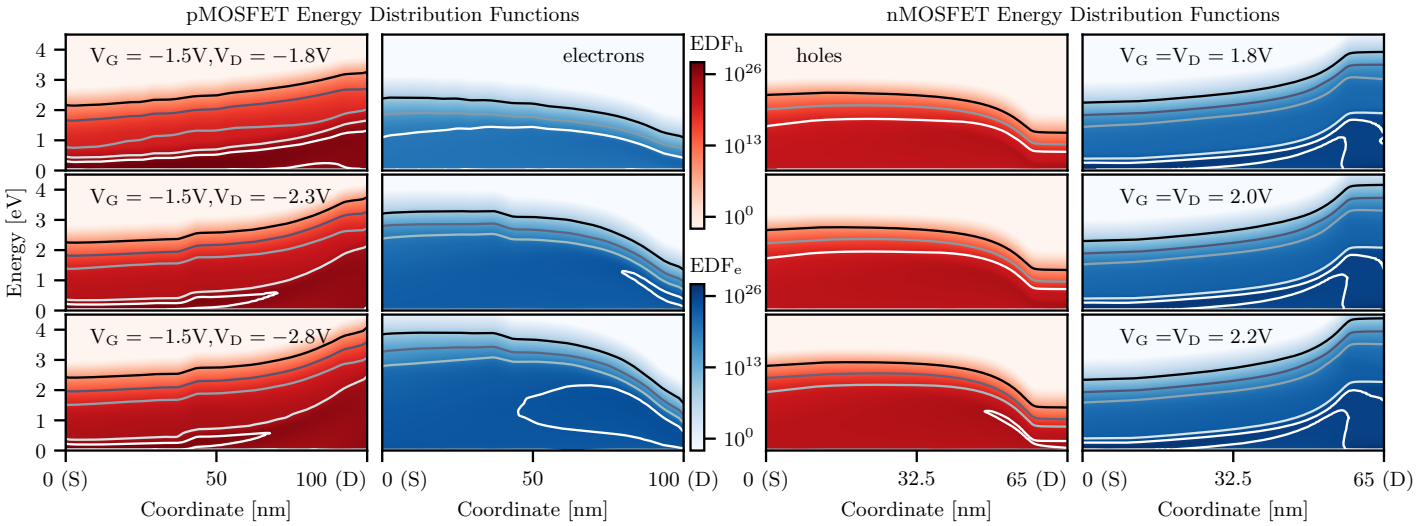

Fig. 9: Energy distribution functions (EDFs) for the pMOSFET (left) and the nMOSFET (right) for various stress regimes obtained from a solution of the bipolar BTE coupled via impact ionization. While the pMOS shows a substantial contribution of secondary generated electrons for increasing stress bias, the hole EDFs for the nMOS remain almost unchanged with varying stress conditions.

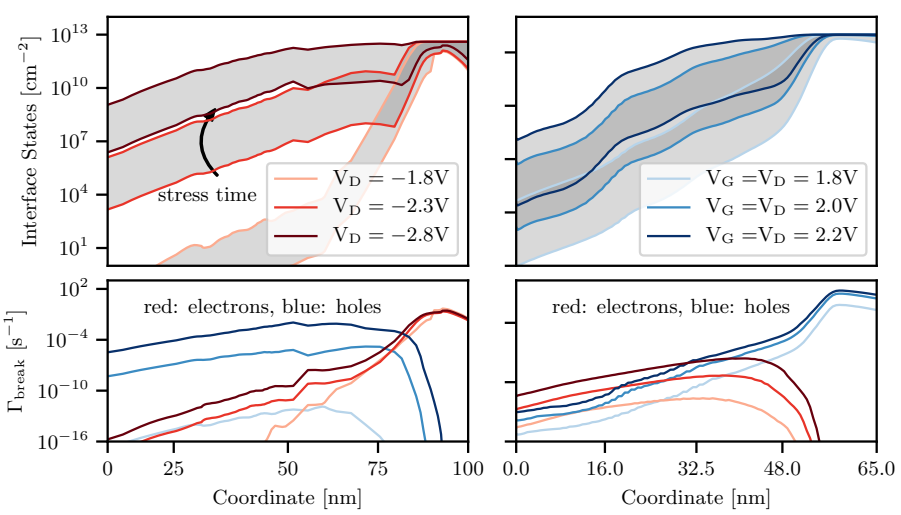

Fig. 10: Interface state profiles, $N_{it}(x)$, for the nMOS and pMOS and all stress combinations between 10 s and 10 ks. Note the increasing damage in the channel region due to electrons created via impact ionization in the pMOSFET. The lower panels give a more detailed picture and show the individual bond breaking rate of holes and electrons along the interface.

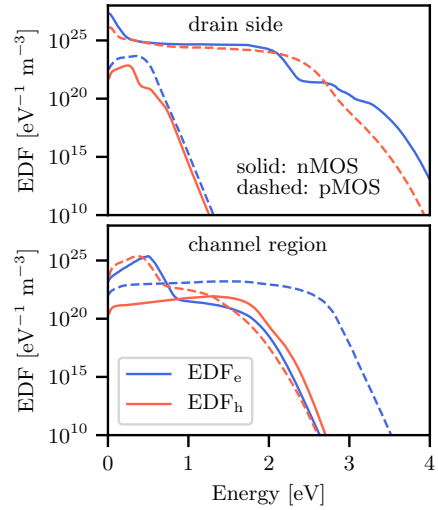

Fig. 11: Comparison with Fig. 10 shows that although similar EDFs are obtained, electrons posses higher bond breaking rates due to the lower resonance level compared to holes and thus create more damage.

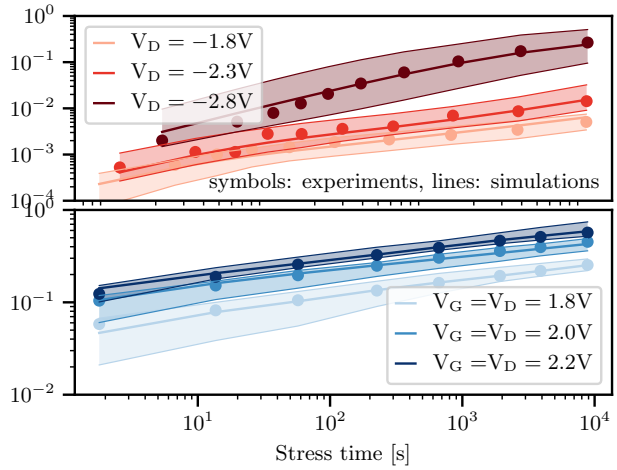

Fig. 12: The presented approach shows excellent agreement with experimental traces. Additionally the model is robust and remains predictive with changes of physical parameters, shaded areas, see Fig. 13.

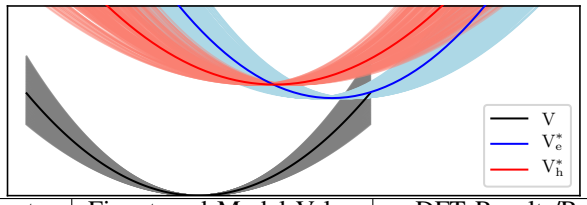

Parameter	Fine–tuned Model Value	DFT Results/Refs.
E_D	2.75 eV	2.77 eV / 2.83 eV [16]
σ_D	0.1 eV	- / 0.08 eV [16]
$E_{res,e}$	3.46 eV	3.67 eV / 4.1 eV [20]
$\Delta_{res,e}$	1.12 eV	1.1 eV / 1.0 eV [21]
$E_{res,h}$	4.45 eV	4.54 eV / 4.8 eV [21]
$\Delta_{res,h}$	0.53 eV	0.56 eV / 0.6 eV [21]
$\tau_{1,0}$	0.78 ns	1.0 ns
σ	2.38×10^{-21} cm^2	- /4 $\times 10^{-21}$ cm^2 [19]

Fig. 13: Optimized model parameter set (within 10%) to account for the real interface structure compared to ab–inito data and literature values which have been used in Fig. 12 to test the stability of our approach. The upper shows the paramter set in terms of the utilized harmonic oscillators.

[1] S. Novak *et al.*, *IRPS* (2015), pp. 2F.2.1–2F.2.5. **[2]** A. Rahman *et al.*, *IRPS* (2018), pp. 6F.4–1–6F.4–6. **[3]** K. Hess *et al.*, Physica E **3**, 1 (1998). **[4]** K. Hess *et al.*, *IEDM* (2000), pp. 93–96. **[5]** W. McMahon *et al.*, *MSM* (2002), pp. 576–579. **[6]** W. McMahon *et al.*, IEEE Trans. Nanotech. **2**, 33 (2003). **[7]** S. Tyaginov *et al.*, EDL **37**, 84 (2016). **[8]** A. Makarov *et al.*, *IEDM* (2017), pp. 13.1.1–13.1.4. **[9]** A. Bravaix *et al.*, *IRPS* (2013), pp. 2D.6.1–2D.6.9. **[10]** J. Franco *et al.*, *IRPS* (2018), pp. 5A.1–1–5A.1–7. **[11]** B. Tuttle *et al.*, Phys. Rev. B **59**, 12884 (1999). **[12]** B. Tuttle, Phys. Rev. B **60**, 2631 (1999). **[13]** C. G. Van de Walle *et al.*, Phys. Rev. B **49**, 14766 (1994). **[14]** C. G. V. de Walle *et al.*, TED **47**, 1779 (2000). **[15]** K. L. Brower, Phys. Rev. B **42**, 3444 (1990). **[16]** A. Stesmans, Phys. Rev. B **61**, 8393 (2000). **[17]** P. Avouris *et al.*, Chem. Phys. Lett. **257**, 148 (1996). **[18]** P. Avouris *et al.*, Surf. Sci. **363**, 368 (1996). **[19]** T. C. Shen, SCIENCE **268**, 1590 (1995). **[20]** K. Stokbro *et al.*, Phys. Rev. Lett. **80**, 2618 (1998). **[21]** K. Stokbro *et al.*, Phys. Rev. B **58**, 8038 (1998). **[22]** B. Persson *et al.*, Surf. Sci. **390**, 45 (1997). **[23]** A. Bravaix *et al.*, *IRPS* (2009), pp. 531–548. **[24]** M. C. Wang *et al.*, EDL **32**, 584 (2011). **[25]** I. Polishchuk *et al.*, TDMR **1**, 158 (2001). **[26]** I. Andrianov *et al.*, J. Chem. Phys. **124**, 34710 (2006). **[27]** C. Guerin *et al.*, J. Appl. Phys. **105**, 114513 (2009). **[28]** M. Houssa *et al.*, Appl. Phys. Lett. **81**, 709 (2002). **[29]** A.-M. El-Sayed *et al.*, Phys. Rev. B **98**, 064102 (2018). **[30]** S.-M. Hong *et al.*, *SISPAD* (2008), pp. 293–296. **[31]** S.-M. Hong *et al.*, J. Comp. Electron **8**, 225 (2009). **[32]** S. Tyaginov *et al.*, *SISPAD* (2011), pp. 123–126. **[33]** J. F. Chen *et al.*, Appl. Phys. Lett. **83**, 1872 (2003).

Acknowledgements: This work was supported in part by by Austrian Science Fund (FWF), grant No. P31204-N30, in part by Austrian Research Promotion Agency FFG (Take off programm, projects no. 861022 and 867414), and in part by the European Union's Horizon 2020 research and innovation programme under the Marie Sklodowska-Curie grant agreement No 794950.